JCB

Supplemental material

Delaney et al., https://doi.org/10.1083/jcb.201811038

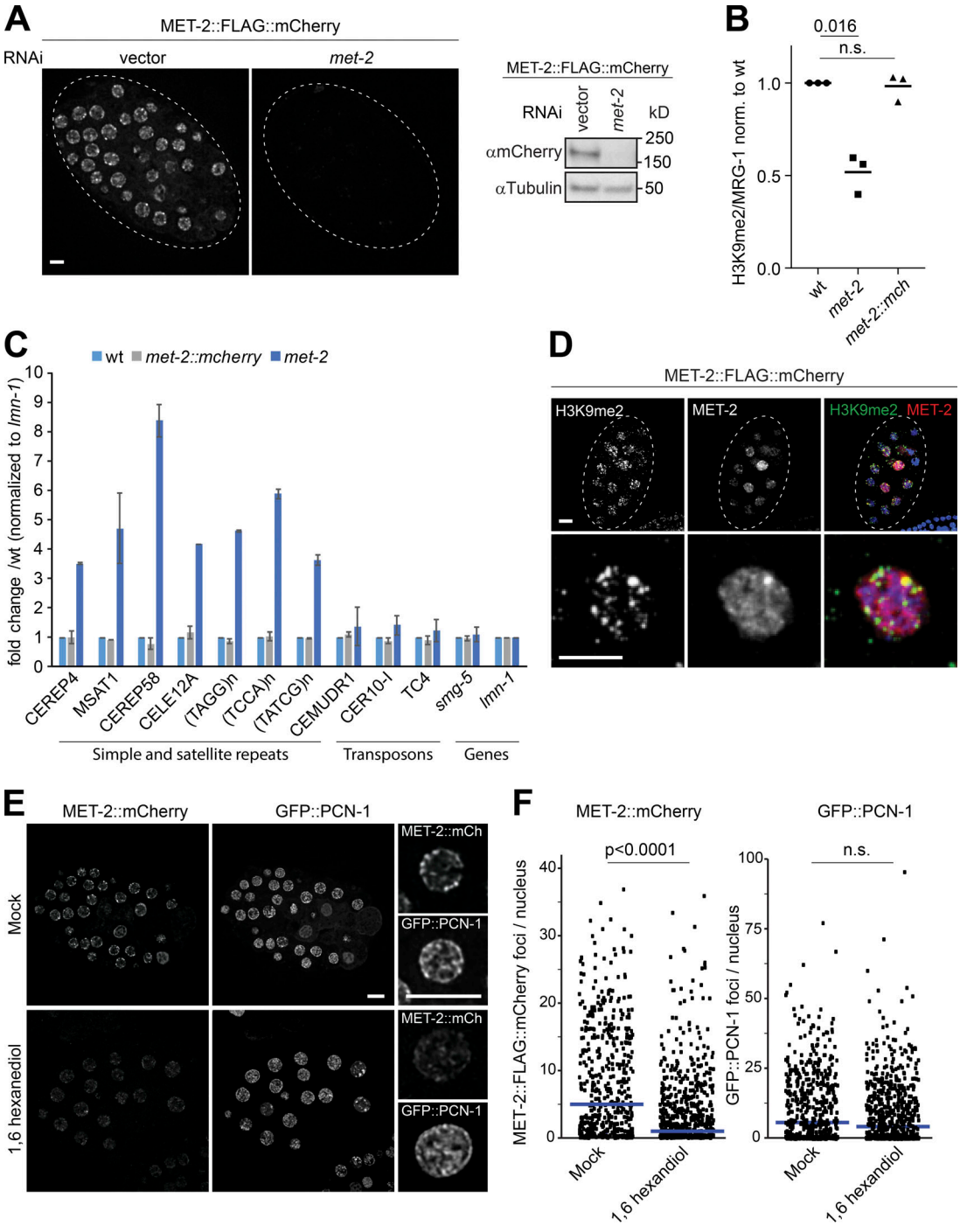

Figure S1. **A fully functional tagged MET-2 protein forms foci that colocalize with repressed H3K9me2 hetrochromatin. (A)** Left: Live-cell image of *met-2::FLAG::mcherry(gw1419)* embryos treated with RNAi targeting *met-2* or empty vector control. Scale bars = 5 µm. Right: Immunoblotting of MET-2::FLAG::mCherry in embryos treated with *met-2* RNAi or vector control. *n* = 3. **(B)** Quantification of H3K9me2 levels from immunoblots shown in Fig. 1 B. Signals in mutants were normalized to wild-type embryos. *n* = 3, P values calculated using two-sided Student *t* test and indicated above the scatterplots; bars indicate mean signal. **(C)** RT-PCR for selected repetitive elements showing the fold change in mRNA level in *met-2(n4256)* and *met-2::flag::mcherry(gw1419)* mixed embryos normalized to levels detected in wild-type mixed embryos (*n* = 3; error bars indicate standard deviation). **(D)** Representative image with IF staining of an early-stage embryo using a specific antibody against H3K9me2 (green; Kimura et al., 2008), and fluorescence signal from mCherry (red) and DAPI in a MET-2::FLAG::mCherry-expressing embryo. Scale bars = 5 µm. **(E)** Representative images of mock (0.1% Triton X-100)-treated and 1,6-hexanediol–treated embryos expressing both MET-2::FLAG::mCherry and GFP::PCN-1. *n* = 3, (mock, *n* = 306; 1,6-hexanediol, *n* = 541). **(F)** Quantification of number of foci in E. Blue bars indicate mean foci number.

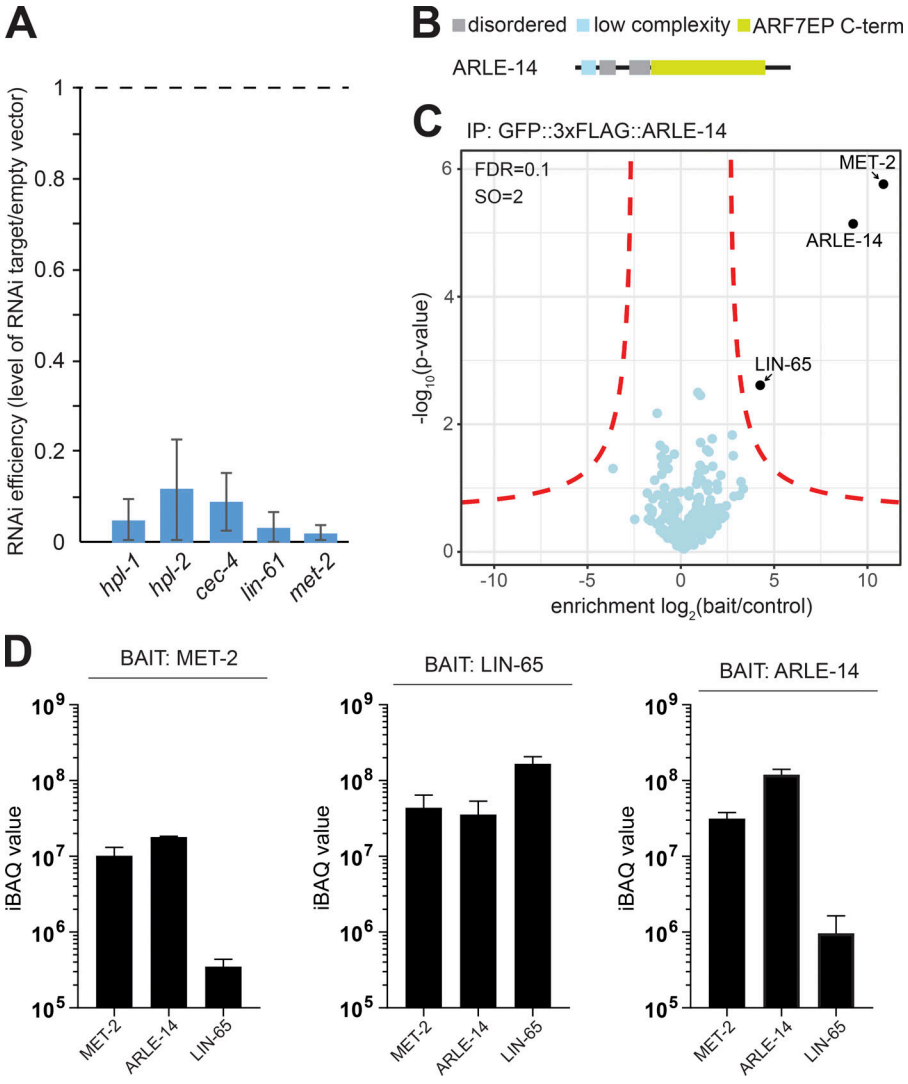

Figure S2. **ARLE-14 and MET-2 interact stochiometrically while LIN-65 is either less stable or substochiometrically bound. (A)** RT-PCR against the indicated genes targeted by RNAi as shown in Fig. 1 (C–F), normalized to vector control expression level. *n* = 3; error bars indicate standard deviation. **(B)** Map of domains of the ARLE-14 protein. **(C)** FLAG-LC-MS/MS of ARLE-14 endogenously tagged with 3xFLAG::GFP. The black circles represent proteins specifically enriched in the pulldown with the tagged strain, and not with the untagged control. Only MET-2, ARLE-14, and LIN-65 are recovered. *n* = 3 biological replicates. Statistical analysis was done with Perseus (see Materials and methods). **(D)** iBAQ values for each enriched protein from immunoprecipitation-MS/MS assays. Bait protein is indicated for each panel. Error bars indicate standard deviation.

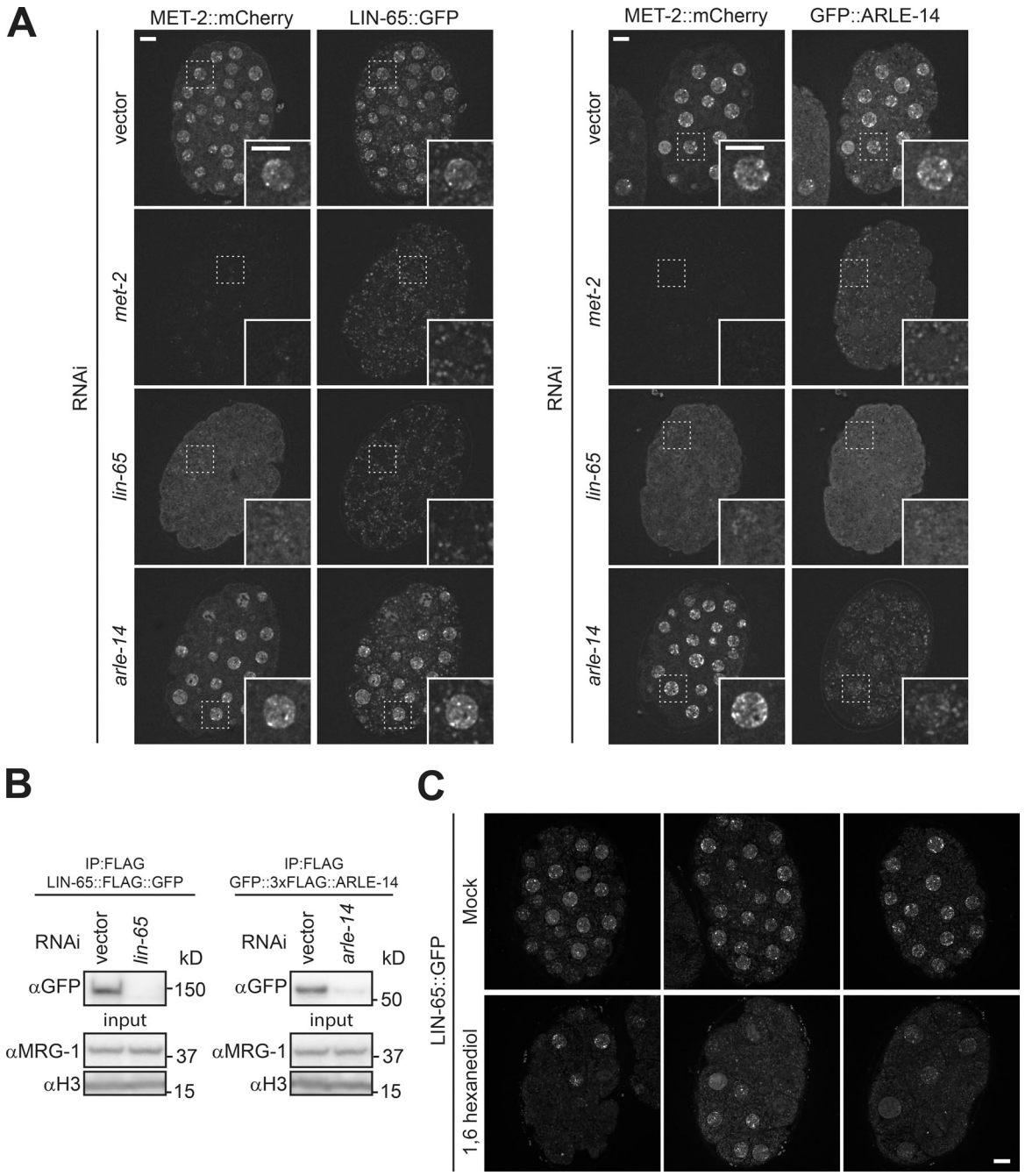

Figure S3. **MET-2 and LIN-65 foci are interdependent and are dispersed by 1,6-hexanediol. (A)** Representative confocal images showing the localization of MET-2::FLAG::mCherry and LIN-65::FLAG::GFP in ∼20-cell-stage embryos treated with RNAi against empty vector (vector), *met-2*, *lin-65*, and *arle-14*. Scale bars = 5 µm. **(B)** Localization of MET-2::FLAG::mCherry and GFP::3xFLAG::ARLE-14 in embryos treated with RNAi against empty vector (vector), *met-2*, *lin-65*, and *arle-14*. Scale bars = 5 µm. **(C)** Immunoblotting of FLAG-immunoprecipitated LIN-65::FLAG::GFP and GFP::3xFLAG::ARLE-14 in embryos treated with *lin-65* and *arle-14* RNAi, respectively, or vector control. Equal volumes of input total protein were used to detect MRG-1 and H3. *n* = 3. **(D)** Three representative images of mock (0.1% Triton X-100)-treated and 1,6-hexanediol–treated embryos expressing LIN-65::FLAG::GFP.

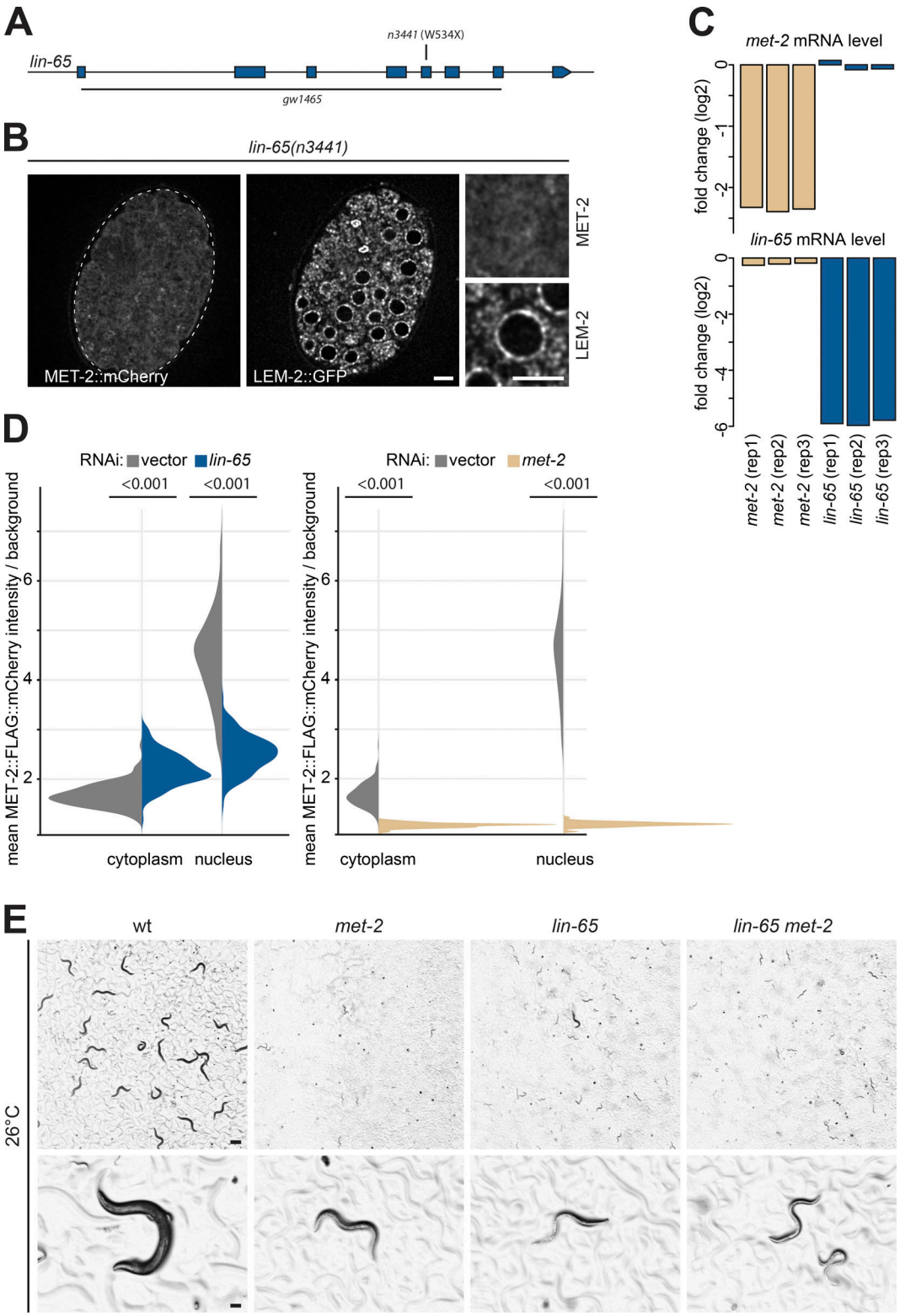

Figure S4. **MET-2 is dispersed between cytoplasm and nucleus in the absence of LIN-65. (A)** Scheme of the *lin-65* gene showing the extent of the deletion in *lin-65(gw1465)* and the point mutant *lin-65(n3441)*. **(B)** Images of MET-2::FLAG::mCherry in wild-type and *lin-65(n3441)* point mutant embryos. Nuclear periphery is visualized with LEM-2::GFP. Scale bar = 5 µm. **(C)** mRNA levels of *met-2* and *lin-65* in either *met-2(n4256)* or *lin-65(gw1465)* mutants, as determined by RNA-seq, show no alteration in transcriptional levels. **(D)** Quantification of MET-2::FLAG::mCherry fluorescence intensity in the cytoplasm and the nucleus of embryos treated with RNAi against *lin-65*, *met-2*, or empty vector (n = 125; P values were calculated using two-sided Wilcoxon signed-rank test and indicated above violin plots). **(E)** Overview and magnification of wild-type, *met-2(n4256)*, *lin-65(gw1465)*, and *lin-65;met-2* mutants grown at 26°C, demonstrating germline sterility of the mutants at the elevated temperature (see also Zeller et al., 2016; Padeken et al., 2019). Scale bars = (upper panel) 500 µm, (lower panel) 50 µm.

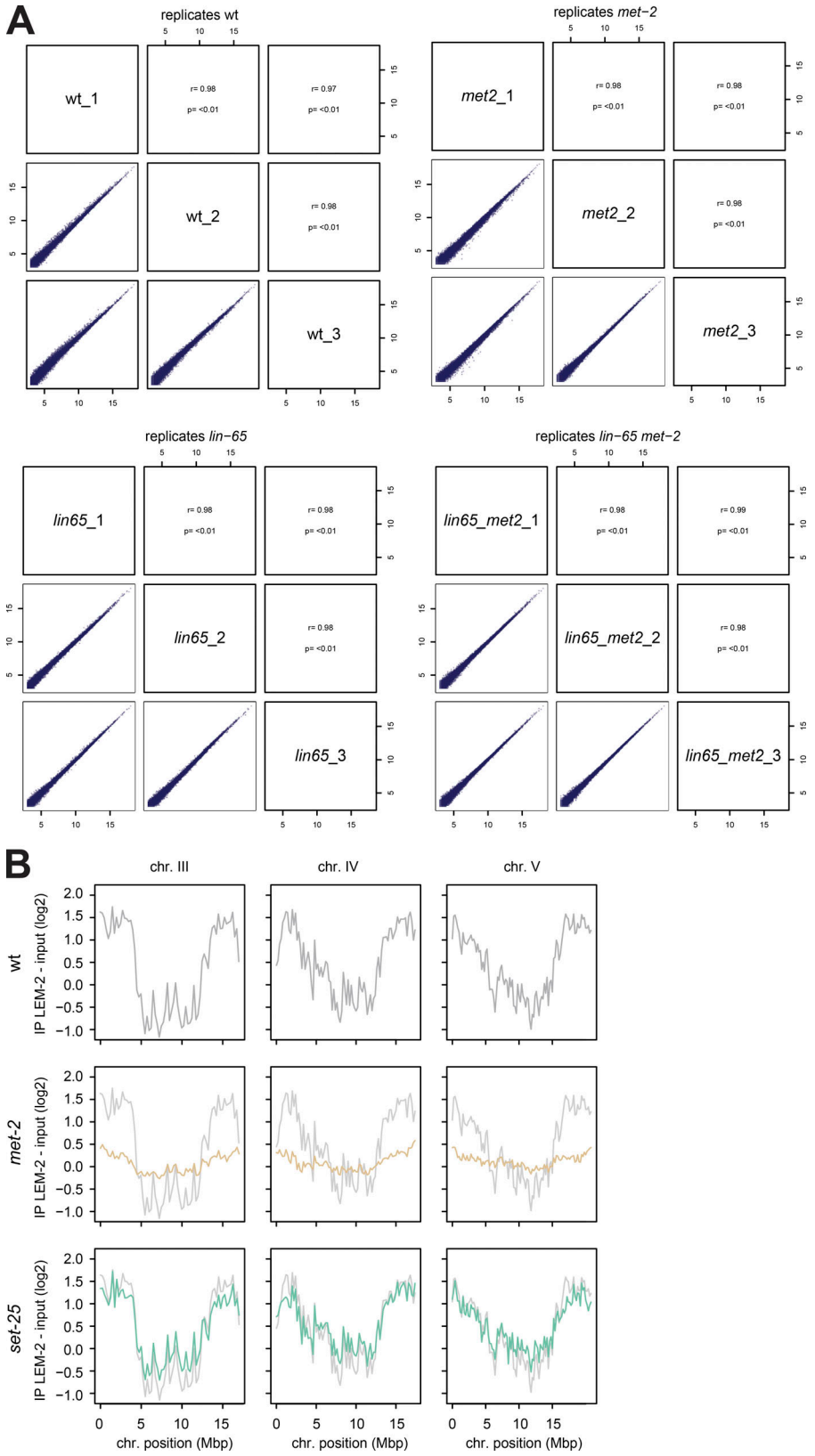

Figure S5. **RNA-seq replicates show strong correlation and perinuclear anchoring is lost in a *met-2* null mutant. (A)** Correlation of the individual replicates from the RNA-seq experiment shown in Fig. 5 for each sequenced genotype. Graphs show the expression of all genes in reads per kilobase per million (RPKM) in log2 for each replica, and the Spearman correlation coefficient is indicate as r to estimate total correlation between replicas. **(B)** Mapping of LEM-2 association with worm chromosomes III–V in wild-type, *met-2(n4256)*, and *set-25(n5021)* mutant by LEM-2 ChIP-seq, as described in Fig. 6.

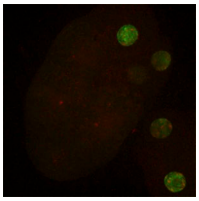

Video 1. Representative video demonstrating the dynamics of MET-2::FLAG::mCherry foci throughout the cell cycle in early embryos. Related to Fig. 1 D. Maximum z-projection, overlay of MET-2 (red) and PCN-1 (green) with 1-min intervals at 5 frames/s.

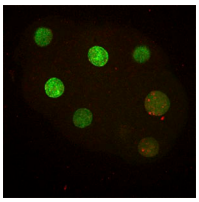

Video 2. Representative video (complementary to Video 1), demonstrating the dynamics of MET-2::FLAG::mCherry foci throughout the cell cycle in early embryos. Related to Fig. 1 D. Maximum z-projection, overlay of MET-2 (red) and PCN-1 (green) with 1-min intervals at 5 frames/s.

Table S1. **Strains used in this study**

Strain	Genotype
GW1	N2 (wild type)
GW76	*gwIs4[Pmyo-3::RFP; Pbaf-1::GFP::lacI::let-858(3′UTR)] X*
GW641	*set-25(n5021)*
GW907	*met-2(n4256)*
GW1419	*met-2::FLAG::TEV::mCherry(gw1419)*
GW1511	*met-2::FLAG::TEV::mCherry(gw1419);gwIs4[Pmyo-3::RFP; Pbaf-1::GFP::lacI::let-858(3′UTR)] X*
GW1539	*gwSi34[lem-2p::lem-2::gfp-3X flag::lem-2 3′UTR] II;met-2::FLAG::TEV::mCherry(gw1419)*
GW1562	*lin-65(gw1465)*
GW1566	*lin-65(gw1465);gwSi34[lem-2p::lem-2::gfp-3X flag::lem-2 3′UTR] II;met-2::FLAG::TEV::mCherry(gw1419)*
GW1571	*lin-65(gw1465);met-2(n4256)*
GW1573	*lin-65(gw1465);met-2::FLAG::TEV::mCherry(gw1419)*
GW1574	*lin-65(n3441)*
GW1576	*met-2::FLAG::TEV::mCherry;isIs17 [pGZ295 (pie-1p::GFP::pcn-1(W03D2.4)) + pDP#MM051 (unc-119(+))]*
GW1580	*lin-65(n3441);met-2::FLAG::TEV::mCherry(gw1419)*
GW1581	*lin-65(n3441);gwSi34[lem-2p::lem-2::gfp-3X flag::lem-2 3′UTR] II;met-2::FLAG::TEV::mCherry(gw1419)*
GW1618	*lin-65::FLAG::TEV::GFP(gw1578)*
GW1621	*lin-65::FLAG::TEV::GFP(gw1578);met-2::FLAG::TEV::mCherry(gw1419)*
GW1623	*GFP::TEV::3xFLAG::arle-14(gw1623);met-2::FLAG::TEV::mCherry(gw1419)*
GW1639	*arle-14(tm6748)*

Table S2. **gRNA sequences**

Target	Guide sequence (5′ to 3′)
met-2 C terminus	TAACTTTTCAGCAAACGGC
lin-65 C terminus	CATTCGAGAGTGATGAAGG
lin-65 5′ end	ATCTGATCATCATTTAATGG
lin-65 3′ end	CGAATTACGATTGTGGCTG
arle-14 N terminus	ATTTGTGCGAGAACGTCAT

References

Kimura, H., Y. Hayashi-Takanaka, Y. Goto, N. Takizawa, and N. Nozaki. 2008. The organization of histone H3 modifications as revealed by a panel of specific monoclonal antibodies. *Cell Struct. Funct.* 33:61–73. https://doi.org/10.1247/csf.07035

Padeken, J., P. Zeller, B. Towbin, I. Katic, V. Kalck, S. Methot, and S.M. Gasser. 2019. Synergistic lethality between BRCA1 and H3K9me2 loss reflects satellite derepression. *Genes Dev.* In press.

Zeller, P., J. Padeken, R. van Schendel, V. Kalck, M. Tijsterman, and S.M. Gasser. 2016. Histone H3K9 methylation is dispensable for *Caenorhabditis elegans* development but suppresses RNA:DNA hybrid-associated repeat instability. *Nat. Genet.* 48:1385–1395. https://doi.org/10.1038/ng.3672